12

Computational Modelling of Auxetics

Bogdan Maruszewski and Tomasz Strek
Poznan University of Technology
Institute of Applied Mechanics
Poland
Artur A. Pozniak
Poznan University of Technology
Institute of Physics
Poland
Krzysztof W. Wojciechowski
PWSZ im. Prezydenta St. Wojciechowskiego w Kaliszu
Poland

1. Introduction

Modern technologies require new materials of special properties. One of the reasons for interest in materials of unusual mechanical properties comes from the fact that they can be used (either as inclusions or as matrices) to form composites of required properties.
There is a number of physical properties that we implicitly assume to be positive. However, one may be surprised to discover that they can also be negative. Negative materials include, amongst other ones, those having negative stiffness (Lakes et al., 2001), negative thermal expansion (Hartwig, 1995), negative refractive index (Sang & Li, 2005), negative permittivity (Ruppin, 2000) and/or negative permeability (Ruppin, 2000). It is worth to add that in presence of some constrains even the compressibility can be negative (Lakes & Wojciechowski, 2008).
A new field of challenge are studies of materials exhibiting negative Poisson's ratio. The latter is a negative ratio of relative transverse dimension change to relative longitudinal dimension change of a body when an infinitesimal change of a stress acting along the longitudinal direction occurs whereas the other stress components remain unchanged. Such materials, first manufactured by Lakes (Lakes, 1987) and coined *auxetics* by Evans (Evans, 1991), are a subject of intensive studies both in the context of fundamental research and applications (Remillat et al., 2009).
The aim of this chapter is to demonstrate recently discovered anomalous deformation of an auxetic plate, constrained by fixing two opposite sides, which is loaded by uniform tension (or compression) applied perpendicularly to two other opposite sides of the plate. The problem was studied both in three dimensions (3D) by Strek et al. (Strek et al., 2008) and in two dimensions (2D) by Pozniak et al. (Pozniak et al., 2010) by finite element methods. In all the cases studied it has been assumed that the material was isotropic.

The paper (Strek et al., 2008) dealt with computer simulations of mechanical behaviour of a thick elastic plate. Simulations have been done for Poisson's ratio from interval $-1 < \nu < 0.5$ using COMSOL (Comsol, 2007). An anomalous feature of the plate deformation for negative Poisson's ratio values compared to classical positive values has been observed at strongly negative Poisson's ratios, $\nu < -0.7$. For such values of ν the displacement vector has components which are anti-parallel to the direction of loading.
2D version of this system, described in (Poźniak et al., 2010), allowed one for more precise computations using much finer meshes than those used in the 3D case. In consequence, the 2D simulations performed with FEniCS (Logg & Wells 2010) revealed the anomalous behaviour of the displacement vector already at $\nu < -0.25$.
The anomalous behaviour of the displacement vector, which in some parts of the plate has components opposite to the direction of the applied force can be thought of as locally negative compliance. Systems with negative compliance have been recently studied by Lakes and co-workers (Lakes, 2001; Lakes et al., 2001; Jaglinski et al., 2007). The reason is that combination of such (negative) materials with common ones (of positive compliance) of the same absolute value offers composites of zero compliance, i.e. of infinite elastic moduli.
In the present chapter we briefly review the results obtained in (Strek et al., 2008) and (Pozniak et al., 2010). By studying larger meshes in 3D and finer ones in 2D we extend those investigations to computationally 'larger' systems. This allows one to study, respectively, thicker plates in 3D and more subtle effects both in 3D and 2D cases. In consequence, we get a better insight in the unusual phenomenon under study.

2. Modelling methods and tools

A great deal of computational research has been undertaken and published in the field of computational mechanics since the advent of the digital computer. Before 1970, the Finite Difference Method (FDM) was almost universally used as a computer based numerical method in modeling dynamics process. Since then there has been a revolution in the general area of mathematical modeling. Highly sophicticated and detailed analysis of many engineering problems has become possible. However, it can be argued that the last three decades have in many ways belonged to the Finite Element Method (FEM) as the method of choice among the currently available numerical methods for solving mathematical equations (Huebner ,1975; Hinton and Owen, 1979).
All mechanical problems considered in this work are governed by equations with appropriate boundary and initial conditions. Numerical results for 3D systems are obtained using standard computational code COMSOL Multiphysics (Comsol, 2004; Comsol, 2007). As COMSOL implicitly simulates 3D systems, to study 2D cases another package, known as FEniCS, was applied. ABAQUS was used to test the obtained results both in 3D and 2D.

2.1 Comsol Multiphysics

Theory in this section is based on COMSOL Multiphysics manual (Comsol, 2007). COMSOL Multiphysics is a powerful interactive environment for modelling and solving all kinds of scientific and engineering problems based on partial differential equations (PDEs) using the finite element method. One can access the power of COMSOL Multiphysics as a standalone product, by script programming in the COMSOL Script language or in the MATLAB language (Comsol, 2007).

A general time-dependent PDE problem in the coefficient form used by COMSOL results in the following equation system (Comsol, 2007)

$$\mathbf{e_a}\frac{\partial^2 \mathbf{u}}{\partial t^2}+\mathbf{d_a}\frac{\partial \mathbf{u}}{\partial t}-\nabla\cdot\left(\mathbf{c}\nabla\mathbf{u}+\boldsymbol{\alpha}\,\mathbf{u}-\boldsymbol{\gamma}\right)+\boldsymbol{\beta}\cdot\nabla\mathbf{u}+\mathbf{a}\,\mathbf{u}=\mathbf{F} \tag{1}$$

with boundary conditions

$$\mathbf{n}\cdot\left(\mathbf{c}\nabla\mathbf{u}+\boldsymbol{\alpha}\,\mathbf{u}-\boldsymbol{\gamma}\right)+\mathbf{q}\,\mathbf{u}=\mathbf{g}-\mathbf{h}^T\boldsymbol{\mu} \tag{2}$$

and

$$\mathbf{hu}=\mathbf{r}\,. \tag{3}$$

The first equation (1) is satisfied inside the domain, whereas the second (2), representing so called generalized Neumann boundary condition, and the third (3) – so called Dirichlet boundary condition, are both satisfied on the boundary of domain. In this work all governing equations obey a general time-dependent PDE problem in the coefficient form reduced to equation

$$-\nabla\cdot\left(\mathbf{c}\nabla\mathbf{u}\right)=\mathbf{F} \tag{4}$$

where the diffusive term flux is defined as

$$\mathbf{c}\nabla\mathbf{u}=\begin{bmatrix}c_{11}&c_{12}&c_{13}\\c_{21}&c_{22}&c_{23}\\c_{31}&c_{32}&c_{33}\end{bmatrix}\nabla\begin{bmatrix}u_1\\u_2\\u_3\end{bmatrix}=\begin{bmatrix}c_{11}&c_{12}&c_{13}\\c_{21}&c_{22}&c_{23}\\c_{31}&c_{32}&c_{33}\end{bmatrix}\cdot\begin{bmatrix}\nabla u_1\\\nabla u_2\\\nabla u_3\end{bmatrix}=\begin{bmatrix}\begin{bmatrix}c_{11}\frac{\partial u_1}{\partial x}+c_{12}\frac{\partial u_2}{\partial x}+c_{13}\frac{\partial u_3}{\partial x}\\c_{11}\frac{\partial u_1}{\partial y}+c_{12}\frac{\partial u_2}{\partial y}+c_{13}\frac{\partial u_3}{\partial y}\\c_{11}\frac{\partial u_1}{\partial z}+c_{12}\frac{\partial u_2}{\partial z}+c_{13}\frac{\partial u_3}{\partial z}\end{bmatrix}\\\begin{bmatrix}c_{21}\frac{\partial u_1}{\partial x}+c_{22}\frac{\partial u_2}{\partial x}+c_{23}\frac{\partial u_3}{\partial x}\\c_{21}\frac{\partial u_1}{\partial y}+c_{22}\frac{\partial u_2}{\partial y}+c_{23}\frac{\partial u_3}{\partial y}\\c_{21}\frac{\partial u_1}{\partial z}+c_{22}\frac{\partial u_2}{\partial z}+c_{23}\frac{\partial u_3}{\partial z}\end{bmatrix}\\\begin{bmatrix}c_{31}\frac{\partial u_1}{\partial x}+c_{32}\frac{\partial u_2}{\partial x}+c_{33}\frac{\partial u_3}{\partial x}\\c_{31}\frac{\partial u_1}{\partial y}+c_{32}\frac{\partial u_2}{\partial y}+c_{33}\frac{\partial u_3}{\partial y}\\c_{31}\frac{\partial u_1}{\partial z}+c_{32}\frac{\partial u_2}{\partial z}+c_{33}\frac{\partial u_3}{\partial z}\end{bmatrix}\end{bmatrix} \tag{5}$$

where ∇u_i are column vectors. The flux matrix or flux tensor is a column vector in this work. For anisotropic materials, each of the components of $\mathbf{c}$ can be a matrix.

2.2 FEniCS

To study 2D systems FEniCS was applied. FEniCS Project (Logg & Wells 2010) is a software suite dedicated to Finite Element Analysis laying emphasis to partial differential equations. DOLFIN may be regarded as its central part being responsible for dealing with the FEM issues. All components of FEniCS are released under GNU General Public License or GNU Lesser General Public License. The sources as well as compiled packages are freely available through http://www.fenics.org.

As mentioned, FEniCS is not a monolithic project but consists of a few components. FIAT is responsible for finite element basis function evaluation. Variational forms coming from weak formulations of PDEs are handled by the Unified Form Language and the FeniCS Form Compiler.

Dealing with FEniCS requires knowledge of the weak forms written in the Unified Form Language in order to let the FEniCS form compiler generate the low level code. Here the bilinear form is written as *a=inner(epsilon(v), sigma(u))*dx* which stands for the integral $\int_X \varepsilon \cdot \sigma dX$, the linear form is *L=inner(v,f)*dx*, representing $\int_X v \cdot F dX$, *v* and *u* are trial and test functions respectively defined in UFL *v=TrialFunction(element), u=TestFunction(element*). Element definition is as simple as previous ones, namely *element=VectorElement("Lagrange","triangle", 1)* for the first order Lagrange element. Putting *a=L* one gets the weak form of differential equation of elasticity.

3. Elastic deformations

3.1 3D case

It is possible to completely describe the strain conditions at a point with the deformation components, (u,v,w) in 3D and their derivatives (Landau and Lifshits, 1986). One can express the shear strain in a tensor form, ε_{xy}, ε_{yz}, ε_{xz} or in an engineering form, γ_{xy}, γ_{yz}, γ_{xz}. Following the small-displacement assumption, the normal strain components and the shear strain components are given from the deformation as follows

$$\begin{aligned} \varepsilon_x &= \frac{\partial u}{\partial x},\ \varepsilon_{xy} = \frac{\gamma_{xy}}{2} = \frac{1}{2}\left(\frac{\partial u}{\partial y} + \frac{\partial v}{\partial x}\right), \\ \varepsilon_y &= \frac{\partial v}{\partial y},\ \varepsilon_{yz} = \frac{\gamma_{yz}}{2} = \frac{1}{2}\left(\frac{\partial v}{\partial z} + \frac{\partial w}{\partial y}\right), \\ \varepsilon_z &= \frac{\partial w}{\partial z},\ \varepsilon_{xz} = \frac{\gamma_{xz}}{2} = \frac{1}{2}\left(\frac{\partial u}{\partial z} + \frac{\partial w}{\partial x}\right). \end{aligned} \tag{6}$$

The symmetric strain tensor, $\boldsymbol{\varepsilon} = \frac{1}{2}\left(\nabla \mathbf{u} + (\nabla \mathbf{u})^T\right)$, consists of both normal and shear strain components

$$\boldsymbol{\varepsilon} = \begin{bmatrix} \varepsilon_{\mathbf{x}} & \varepsilon_{\mathbf{x}y} & \varepsilon_{\mathbf{x}z} \\ \varepsilon_{y\mathbf{x}} & \varepsilon_{y} & \varepsilon_{yz} \\ \varepsilon_{z\mathbf{x}} & \varepsilon_{zy} & \varepsilon_{z} \end{bmatrix}. \tag{7}$$

The stress in a material is described by the symmetric stress tensor $\boldsymbol{\sigma}$

$$\boldsymbol{\sigma} = \begin{bmatrix} \sigma_x & \tau_{xy} & \tau_{xz} \\ \tau_{yx} & \sigma_y & \tau_{yz} \\ \tau_{zx} & \tau_{zy} & \sigma_z \end{bmatrix} \tag{8}$$

consisting of three normal stresses $(\sigma_x, \sigma_y, \sigma_z)$ and six, or if symmetry is used, three shear stresses $(\tau_{xy}, \tau_{yz}, \tau_{xz})$. The stress-strain relationship (the constitutive law) for linear conditions reads

$$\boldsymbol{\sigma} = \mathbf{D}\varepsilon \tag{9}$$

where $\mathbf{D}$ is a 6 x 6 elasticity matrix, and the stress and strain components are described in vector form with the six stress and strain components in column vectors defined as

$$\begin{aligned} \sigma &= \left[\sigma_x, \sigma_y, \sigma_z, \tau_{xy}, \tau_{yz}, \tau_{xz}\right]^T, \\ \varepsilon &= \left[\varepsilon_x, \varepsilon_y, \varepsilon_z, \gamma_{xy}, \gamma_{yz}, \gamma_{xz}\right]^T. \end{aligned} \tag{10}$$

For static conditions Navier's equation reads (Landau and Lifshits, 1986)

$$-\nabla \cdot \boldsymbol{\sigma} = \mathbf{F} \tag{11}$$

where **u** denotes the displacement and $\mathbf{F}$ denotes the volume forces (body forces).

Lamé's constants λ and μ in terms of Young's modulus, E, and Poisson's ratio, ν, are the following

$$\begin{aligned} \lambda &= \frac{E\nu}{(1+\nu)(1-2\nu)}, \\ \mu &= \frac{E}{2(1+\nu)}, \end{aligned} \tag{12}$$

then the elastic matrix $\mathbf{D}$ reads

$$\mathbf{D}=\frac{E}{(1+\nu)(1-2\nu)}\begin{bmatrix}1-\nu & \nu & \nu & 0 & 0 & 0\\ \nu & 1-\nu & \nu & 0 & 0 & 0\\ \nu & \nu & 1-\nu & 0 & 0 & 0\\ 0 & 0 & 0 & \frac{1-2\nu}{2} & 0 & 0\\ 0 & 0 & 0 & 0 & \frac{1-2\nu}{2} & 0\\ 0 & 0 & 0 & 0 & 0 & \frac{1-2\nu}{2}\end{bmatrix}. \tag{13}$$

The use of (7)–(10) in (6) leads us to Navier's equation - the final form of the equation (Comsol, 2004; Comsol, 2007)

$$-\nabla\cdot(\mathbf{c}\nabla\mathbf{u})=\mathbf{F}\,, \tag{14}$$

where $\mathbf{c}$ is the flux matrix. The flux matrix $\mathbf{c}$ reads

$$\mathbf{c}=\begin{bmatrix}\begin{bmatrix}D_{11} & D_{14} & D_{16}\\ D_{14} & D_{44} & D_{46}\\ D_{16} & D_{46} & D_{66}\end{bmatrix} & \begin{bmatrix}D_{14} & D_{12} & D_{15}\\ D_{44} & D_{24} & D_{45}\\ D_{46} & D_{26} & D_{56}\end{bmatrix} & \begin{bmatrix}D_{16} & D_{15} & D_{13}\\ D_{46} & D_{45} & D_{34}\\ D_{66} & D_{56} & D_{36}\end{bmatrix}\\ \begin{bmatrix}D_{14} & D_{44} & D_{46}\\ D_{12} & D_{24} & D_{26}\\ D_{15} & D_{45} & D_{56}\end{bmatrix} & \begin{bmatrix}D_{44} & D_{24} & D_{45}\\ D_{24} & D_{22} & D_{25}\\ D_{45} & D_{25} & D_{55}\end{bmatrix} & \begin{bmatrix}D_{46} & D_{45} & D_{34}\\ D_{26} & D_{25} & D_{23}\\ D_{56} & D_{55} & D_{35}\end{bmatrix}\\ \begin{bmatrix}D_{16} & D_{46} & D_{66}\\ D_{15} & D_{45} & D_{56}\\ D_{13} & D_{34} & D_{36}\end{bmatrix} & \begin{bmatrix}D_{46} & D_{26} & D_{56}\\ D_{45} & D_{25} & D_{55}\\ D_{34} & D_{23} & D_{35}\end{bmatrix} & \begin{bmatrix}D_{66} & D_{56} & D_{36}\\ D_{56} & D_{55} & D_{35}\\ D_{36} & D_{35} & D_{33}\end{bmatrix}\end{bmatrix}. \tag{15}$$

D_{ij} in the $\mathbf{c}$ matrix is referring to the component in the elasticity matrix (13) in the stress-strain relation for 3D.

In this case, the diffusive flux, reads

$$\mathbf{c}\nabla\mathbf{u}=\begin{bmatrix}\begin{bmatrix}D_{11} & D_{14} & D_{16}\\ D_{14} & D_{44} & D_{46}\\ D_{16} & D_{46} & D_{66}\end{bmatrix} & \begin{bmatrix}D_{14} & D_{12} & D_{15}\\ D_{44} & D_{24} & D_{45}\\ D_{46} & D_{26} & D_{56}\end{bmatrix} & \begin{bmatrix}D_{16} & D_{15} & D_{13}\\ D_{46} & D_{45} & D_{34}\\ D_{66} & D_{56} & D_{36}\end{bmatrix}\\ \begin{bmatrix}D_{14} & D_{44} & D_{46}\\ D_{12} & D_{24} & D_{26}\\ D_{15} & D_{45} & D_{56}\end{bmatrix} & \begin{bmatrix}D_{44} & D_{24} & D_{45}\\ D_{24} & D_{22} & D_{25}\\ D_{45} & D_{25} & D_{55}\end{bmatrix} & \begin{bmatrix}D_{46} & D_{45} & D_{34}\\ D_{26} & D_{25} & D_{23}\\ D_{56} & D_{55} & D_{35}\end{bmatrix}\\ \begin{bmatrix}D_{16} & D_{46} & D_{66}\\ D_{15} & D_{45} & D_{56}\\ D_{13} & D_{34} & D_{36}\end{bmatrix} & \begin{bmatrix}D_{46} & D_{26} & D_{56}\\ D_{45} & D_{25} & D_{55}\\ D_{34} & D_{23} & D_{35}\end{bmatrix} & \begin{bmatrix}D_{66} & D_{56} & D_{36}\\ D_{56} & D_{55} & D_{35}\\ D_{36} & D_{35} & D_{33}\end{bmatrix}\end{bmatrix}\begin{bmatrix}\nabla u_1\\ \nabla u_2\\ \nabla u_3\end{bmatrix}. \tag{16}$$

After some mathematical calculations one can write equation (16) in the following form

$$\mathbf{c}\nabla\mathbf{u} = \begin{bmatrix} \begin{bmatrix} D_{11} & D_{14} & D_{16} \\ D_{14} & D_{44} & D_{46} \\ D_{16} & D_{46} & D_{66} \end{bmatrix} \nabla u_1 + \begin{bmatrix} D_{14} & D_{12} & D_{15} \\ D_{44} & D_{24} & D_{45} \\ D_{46} & D_{26} & D_{56} \end{bmatrix} \nabla u_2 + \begin{bmatrix} D_{16} & D_{15} & D_{13} \\ D_{46} & D_{45} & D_{34} \\ D_{66} & D_{56} & D_{36} \end{bmatrix} \nabla u_3 \\ \begin{bmatrix} D_{14} & D_{44} & D_{46} \\ D_{12} & D_{24} & D_{26} \\ D_{15} & D_{45} & D_{56} \end{bmatrix} \nabla u_1 + \begin{bmatrix} D_{44} & D_{24} & D_{45} \\ D_{24} & D_{22} & D_{25} \\ D_{45} & D_{25} & D_{55} \end{bmatrix} \nabla u_2 + \begin{bmatrix} D_{46} & D_{45} & D_{34} \\ D_{26} & D_{25} & D_{23} \\ D_{56} & D_{55} & D_{35} \end{bmatrix} \nabla u_3 \\ \begin{bmatrix} D_{16} & D_{46} & D_{66} \\ D_{15} & D_{45} & D_{56} \\ D_{13} & D_{34} & D_{36} \end{bmatrix} \nabla u_1 + \begin{bmatrix} D_{46} & D_{26} & D_{56} \\ D_{45} & D_{25} & D_{55} \\ D_{34} & D_{23} & D_{35} \end{bmatrix} \nabla u_2 + \begin{bmatrix} D_{66} & D_{56} & D_{36} \\ D_{56} & D_{55} & D_{35} \\ D_{36} & D_{35} & D_{33} \end{bmatrix} \nabla u_3 \end{bmatrix} = \begin{bmatrix} \begin{bmatrix} \alpha_{11} \\ \alpha_{12} \\ \alpha_{13} \end{bmatrix} \\ \begin{bmatrix} \alpha_{21} \\ \alpha_{22} \\ \alpha_{23} \end{bmatrix} \\ \begin{bmatrix} \alpha_{31} \\ \alpha_{32} \\ \alpha_{33} \end{bmatrix} \end{bmatrix}. \tag{17}$$

For example, the component α_{11} reads

$$\begin{aligned} \alpha_{11} &= D_{11}\frac{\partial u_1}{\partial x_1} + D_{14}\frac{\partial u_1}{\partial x_2} + D_{16}\frac{\partial u_1}{\partial x_3} \\ &+ D_{14}\frac{\partial u_2}{\partial x_1} + D_{12}\frac{\partial u_2}{\partial x_2} + D_{15}\frac{\partial u_2}{\partial x_3} \\ &+ D_{16}\frac{\partial u_3}{\partial x_1} + D_{15}\frac{\partial u_3}{\partial x_2} + D_{13}\frac{\partial u_3}{\partial x_3} \end{aligned}. \tag{18}$$

The remaining components α_{ij} one can calculate similarly.

For the flux terms the divergence operator works on each row separately. The divergence of the conservative flux source reads

$$\nabla\cdot\boldsymbol{\alpha} = \nabla\cdot\begin{bmatrix} \begin{bmatrix} \alpha_{11} \\ \alpha_{12} \\ \alpha_{13} \end{bmatrix} \\ \begin{bmatrix} \alpha_{21} \\ \alpha_{22} \\ \alpha_{23} \end{bmatrix} \\ \begin{bmatrix} \alpha_{31} \\ \alpha_{32} \\ \alpha_{33} \end{bmatrix} \end{bmatrix} = \begin{bmatrix} \nabla\cdot\begin{bmatrix} \alpha_{11} \\ \alpha_{12} \\ \alpha_{13} \end{bmatrix} \\ \nabla\cdot\begin{bmatrix} \alpha_{21} \\ \alpha_{22} \\ \alpha_{23} \end{bmatrix} \\ \nabla\cdot\begin{bmatrix} \alpha_{31} \\ \alpha_{32} \\ \alpha_{33} \end{bmatrix} \end{bmatrix} = \begin{bmatrix} \frac{\partial\alpha_{11}}{\partial x_1} + \frac{\partial\alpha_{12}}{\partial x_2} + \frac{\partial\alpha_{13}}{\partial x_3} \\ \frac{\partial\alpha_{21}}{\partial x_1} + \frac{\partial\alpha_{22}}{\partial x_2} + \frac{\partial\alpha_{23}}{\partial x_3} \\ \frac{\partial\alpha_{31}}{\partial x_1} + \frac{\partial\alpha_{32}}{\partial x_2} + \frac{\partial\alpha_{33}}{\partial x_3} \end{bmatrix}. \tag{19}$$

3.2 2D case

In consequence of the dimension reduction from 3D to 2D one has to modify eq. (12). In a two-dimensional world λ takes the following form

$$\lambda = \frac{E\nu}{(1+\nu)(1-\nu)}, \tag{20}$$

as Poisson's ratio fits the range $\nu \in <-1;1>$. Expression for μ remains unchanged.
Obviously, in 2D, vectors have two components, instead of three, and one works with 2x2 matrices, instead of 3x3.

4. Numerical results

4.1 3D case

The object of our interest is a box in 3D, fixed at two parallel lateral surfaces (see Fig. 1C) and loaded at front and back (see Fig. 1A) parallel opposite surfaces. The top and the bottom (parallel) walls are free (Fig. 1B). Four cases of box shape have been considered (see Table 2). Boxes were made either of classic (Poisson's ratio: 0 and +0.3) or auxetic material (Poisson's ratio: -0.999999 and -0.7), isotropic and elastic loaded. In all cases extensions of the box were considered. Numerical data necessary to perform the calculations are collected in Table 1.
All the calculations have been done by Comsol Multiphysics code (Comsol, 2007). Finite element calculations are made with second-order tetrahedral Lagrange elements with mesh statistics collected in Table 2.
Firstly, static Navier's equation is analyzed in this chapter. The following boundary conditions are assumed:

- Loaded boundary - for $x = 0 : \boldsymbol{\sigma} \cdot \mathbf{n} = -\mathbf{P}$, $\mathbf{P} \neq \mathbf{0}$,
- Loaded boundary - for $x = L : \boldsymbol{\sigma} \cdot \mathbf{n} = \mathbf{P}$,
- Fixed boundary - for $y = 0$ and $y = d : \mathbf{u} = \mathbf{0}$,
- Free boundary - for $z = 0$ and $z = h$,

where $\mathbf{n}$ is the normal unit vector to boundary.
There is no initial stress and strain in the considered boxes.
Results concerning the simulations of the stretched boxes are shown in Fig 3-12. An anomalous feature of the box deformation for negative Poisson's ratio values compared to classical positive values has been observed. At extremely negative Poisson's ratios the displacement vector has components which are anti-parallel to the direction of loading. This feature is present for all considered boxes with different ratios of height to depth.

Quantity	Symbol	Unit	Value
Density	ρ	kg/m^3	7850
Young's modulus	E	Pa	$2.1 \cdot 10^{11}$
Poisson's ratio	ν	-	-0.999999, -0.7, 0, 0.3
Pressure – force per area (stretch)	$\lvert\mathbf{P}\rvert$	N/m^2	10^4

Table 1. Numerical data

Quantity	Symbol	Unit	Box-1	Box-2	Box-3	Box-4
Height (z-direction)	h	m	2	1	0.5	0.005
Width (x-direction)	L	m	1	1	1	1
Depth (y-direction)	d	m	1	1	1	1
Number of mesh points	-	-	27642	12186	6096	139386
Number of elements	-	-	143682	61126	29605	523183
Number of DOF	-	-	607137	262377	129219	2675307

Table 2. Dimensions of boxes and mesh statistics

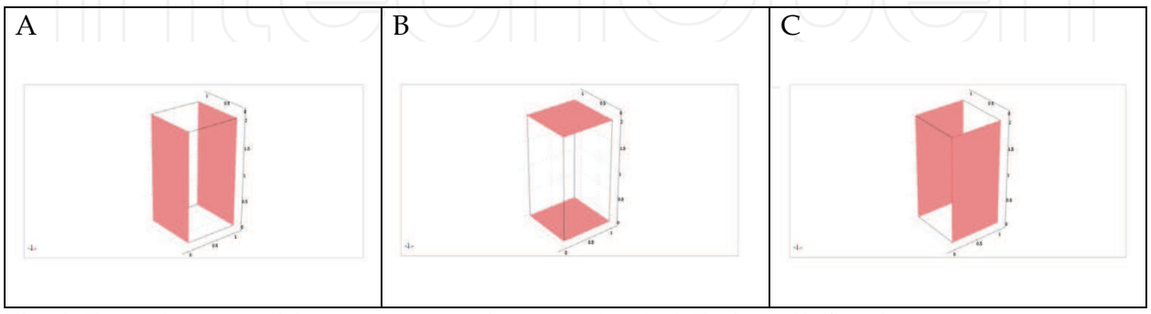

Fig. 1. Boundary conditions on box surfaces: A) loaded, B) free, C) fixed

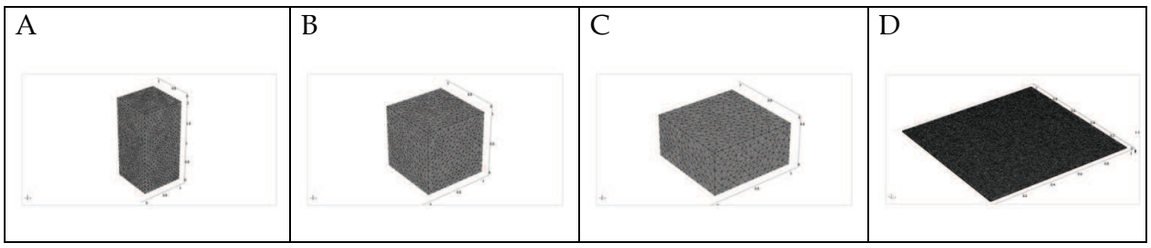

Fig. 2. Shapes of meshed boxes: A) Box-1, B) Box-2, C) Box-3, D) Box-4

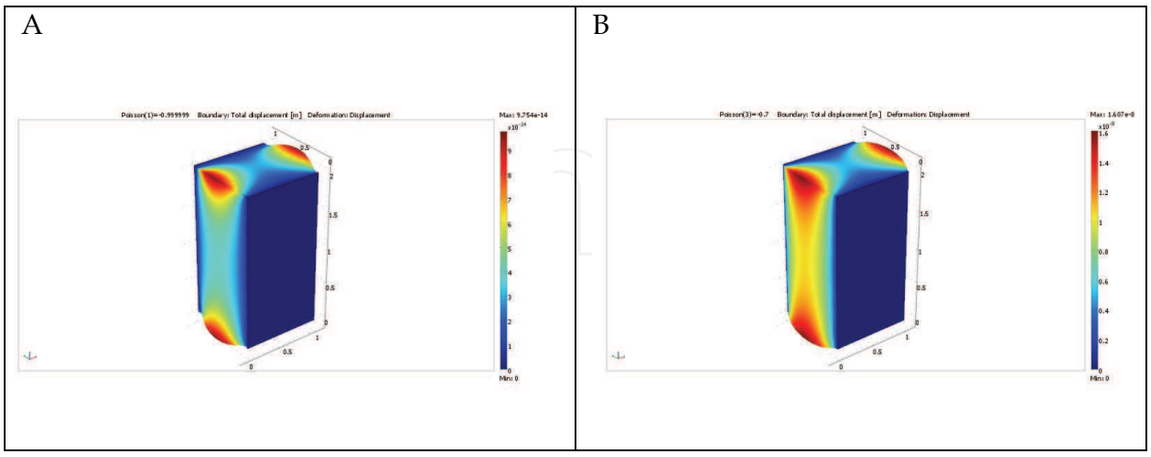

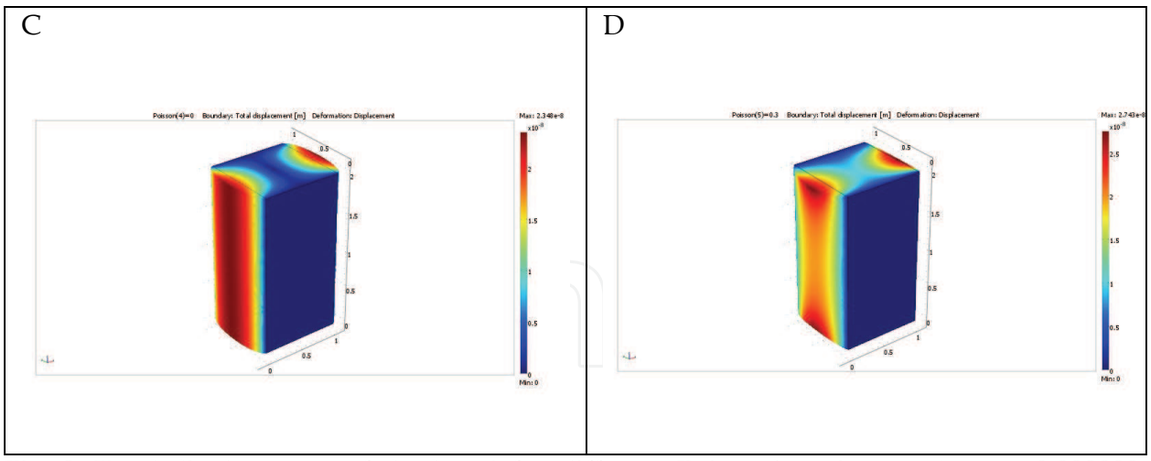

Fig. 3. Total displacement of the box-1 for different Poisson's ratios ν: A) ν = -0.999999, B) ν = -0.7, C) ν = 0, D) ν = 0.3. The initial shape of the plate is marked by a thin continuous line

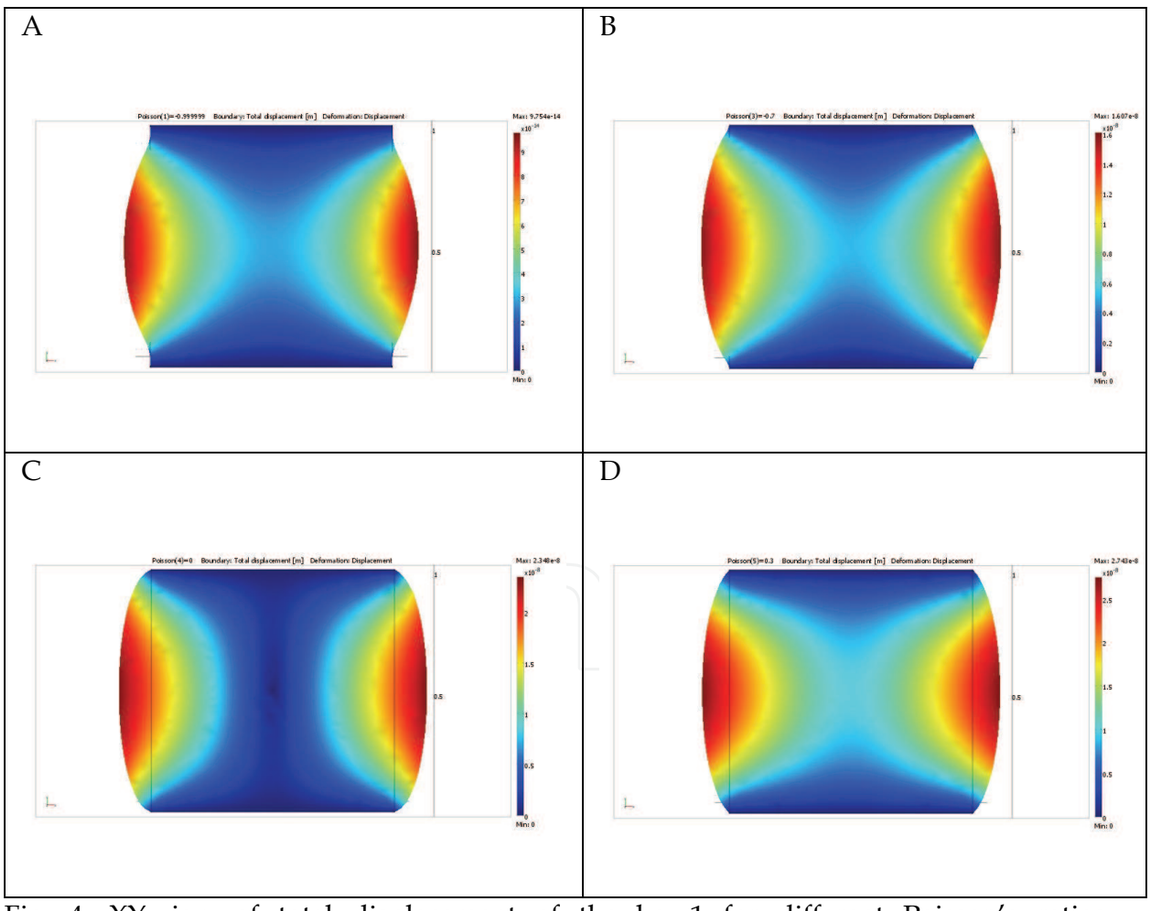

Fig. 4. XY-view of total displacement of the box-1 for different Poisson's ratios ν: A) ν = -0.999999, B) ν = -0.7, C) ν = 0, D) ν = 0.3

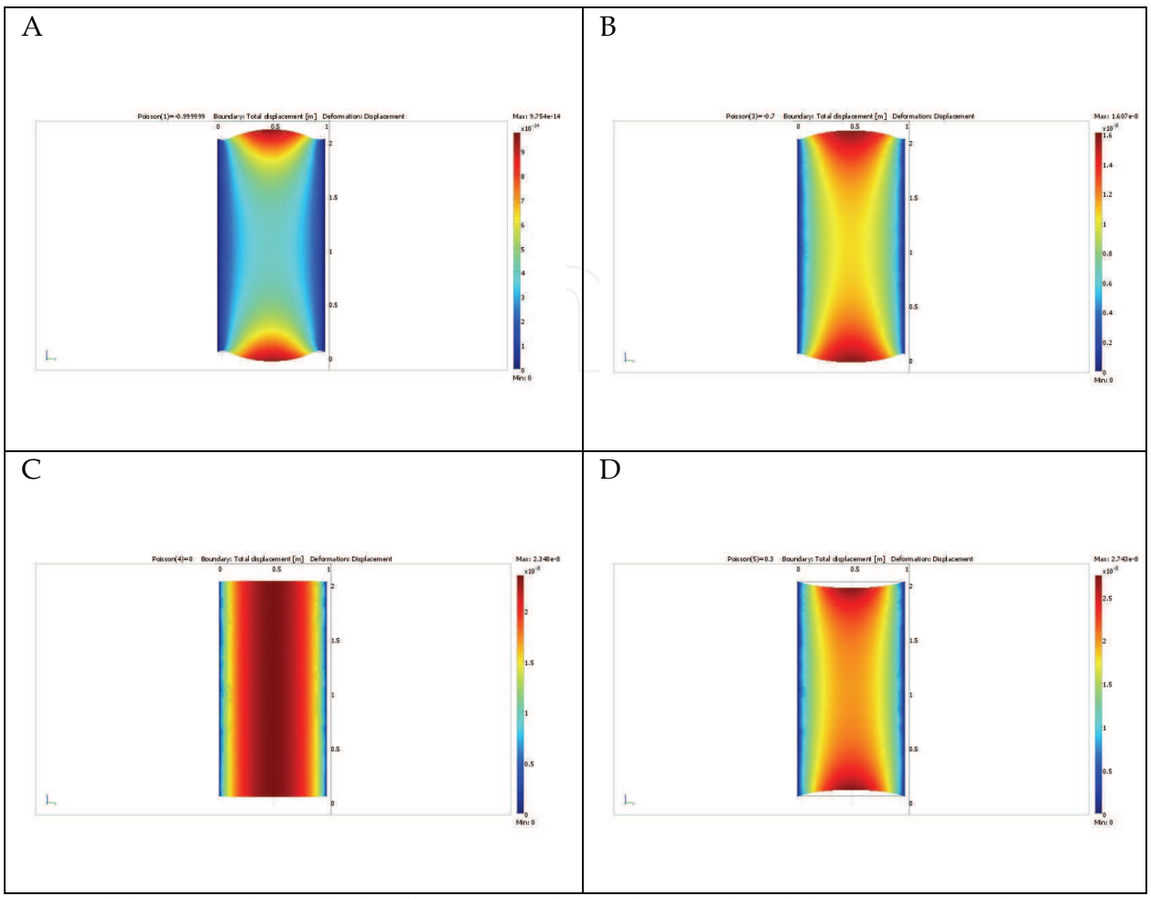

Fig. 5. YZ-view of total displacement of the box-1 for different Poisson's ratios ν: A) ν = -0.999999, B) ν = -0.7, C) ν = 0, D) ν = 0.3

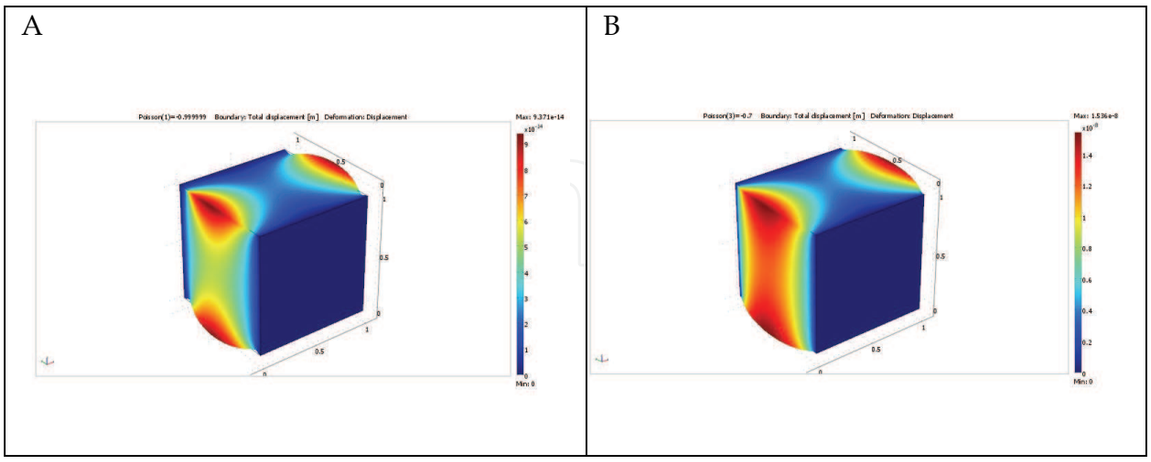

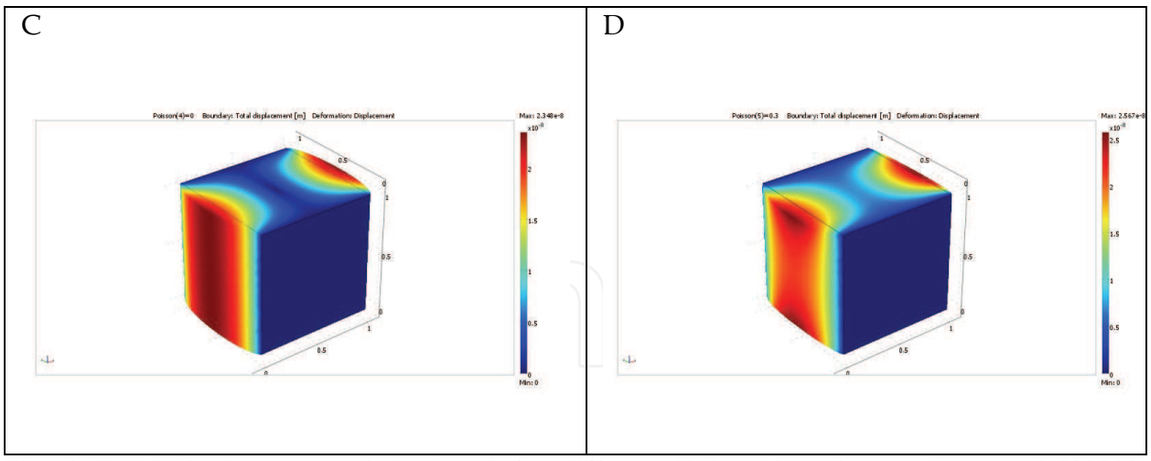

Fig. 6. Total displacement of the box-2 for different Poisson's ratios v: A) v = -0.999999, B) v = -0.7, C) v = 0, D) v = 0.3

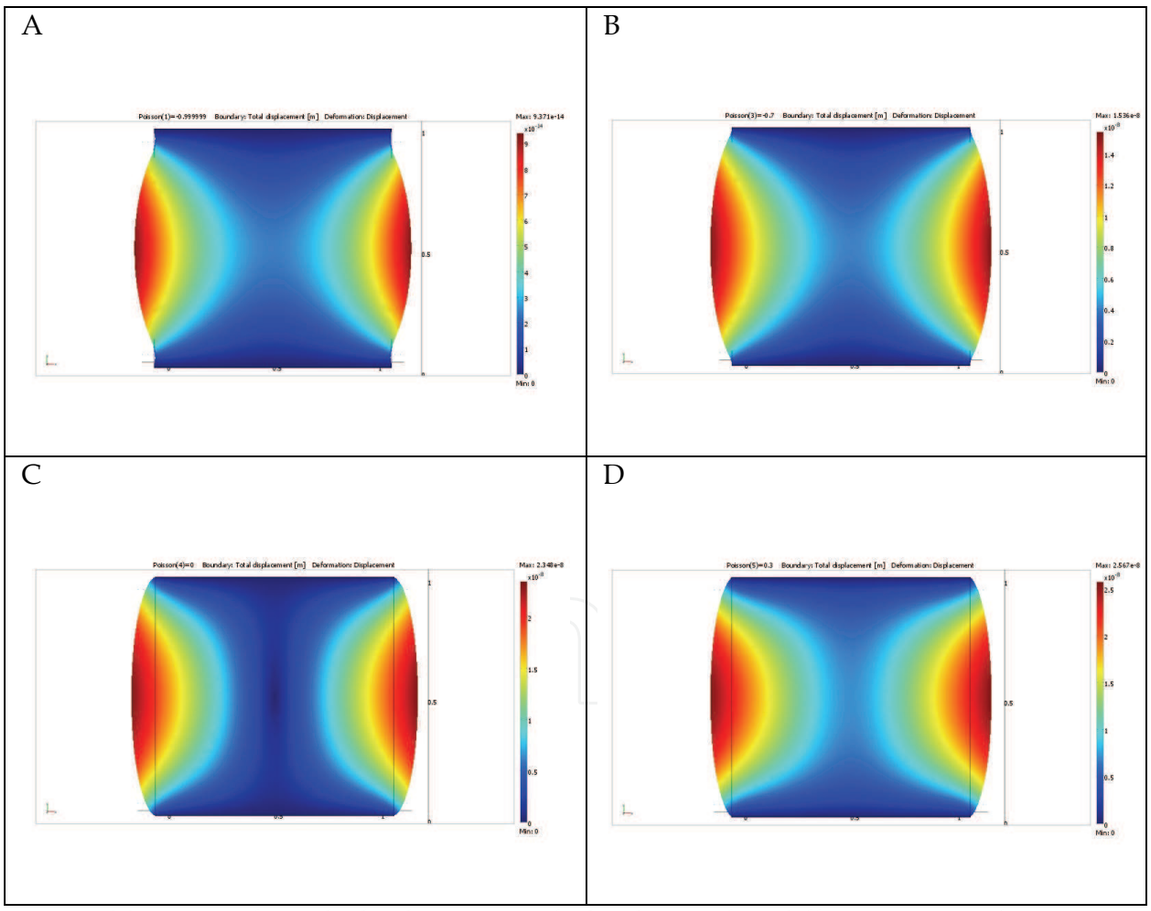

Fig. 7. XY-view of total displacement of the box-2 for different Poisson's ratios v: A) v = -0.999999, B) v = -0.7, C) v = 0, D) v = 0.3

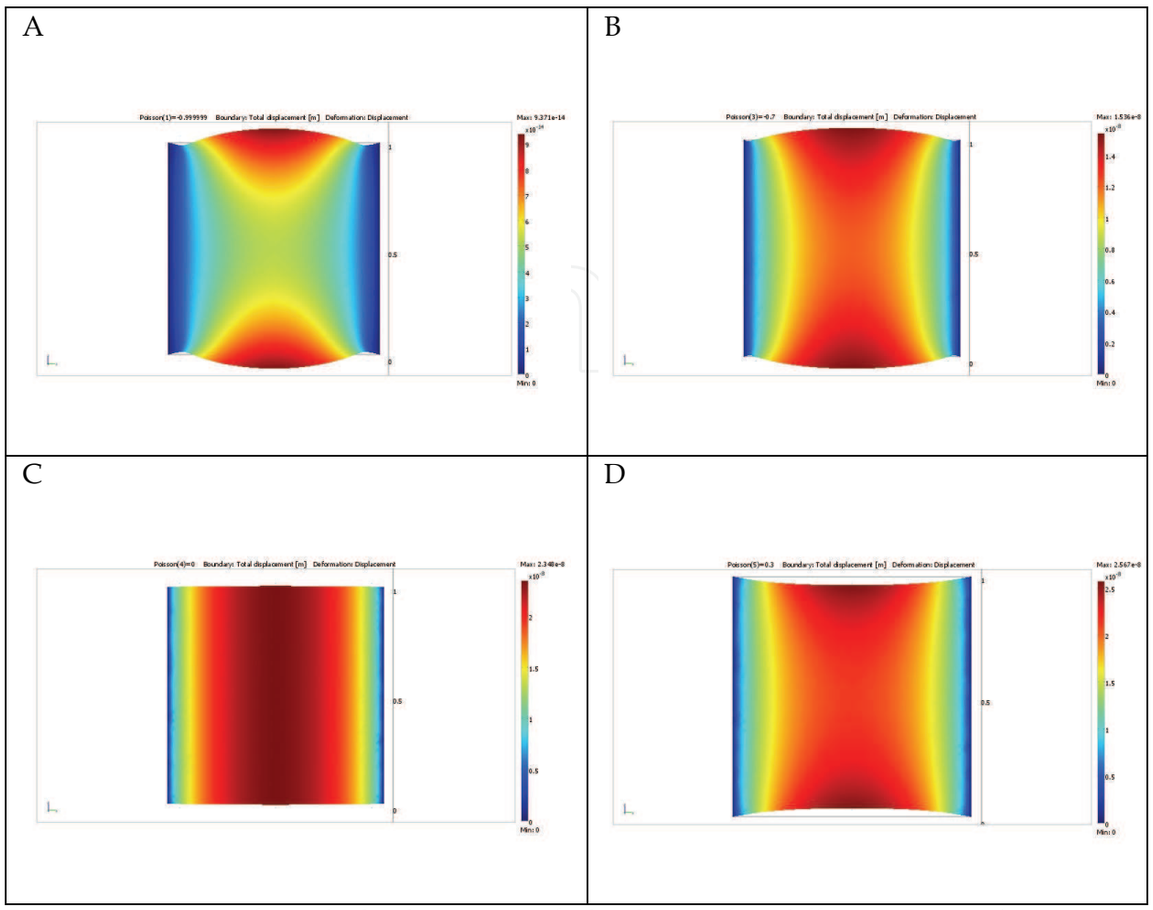

Fig. 8. YZ-view of total displacement of the box-2 for different Poisson's ratios v: A) v = -0.999999, B) v = -0.7, C) v = 0, D) v = 0.3

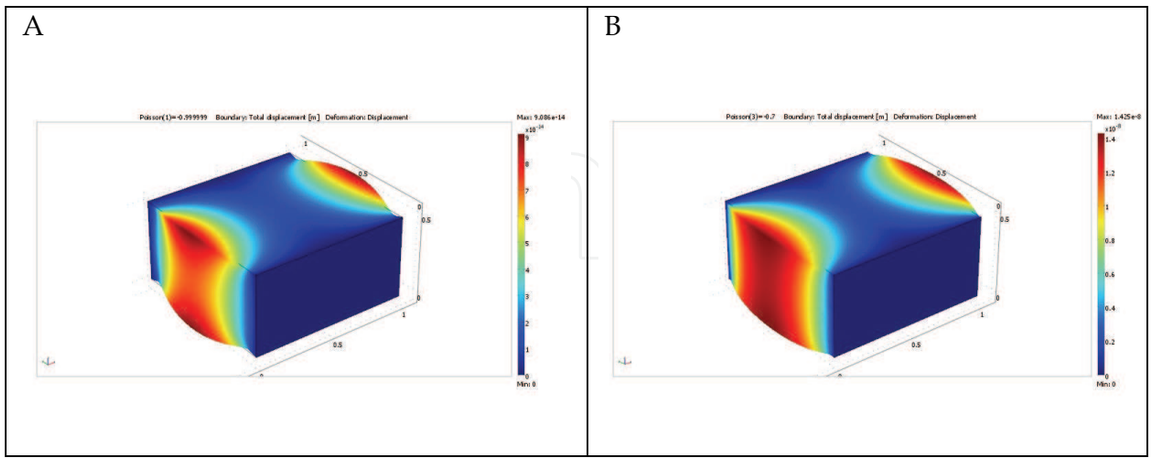

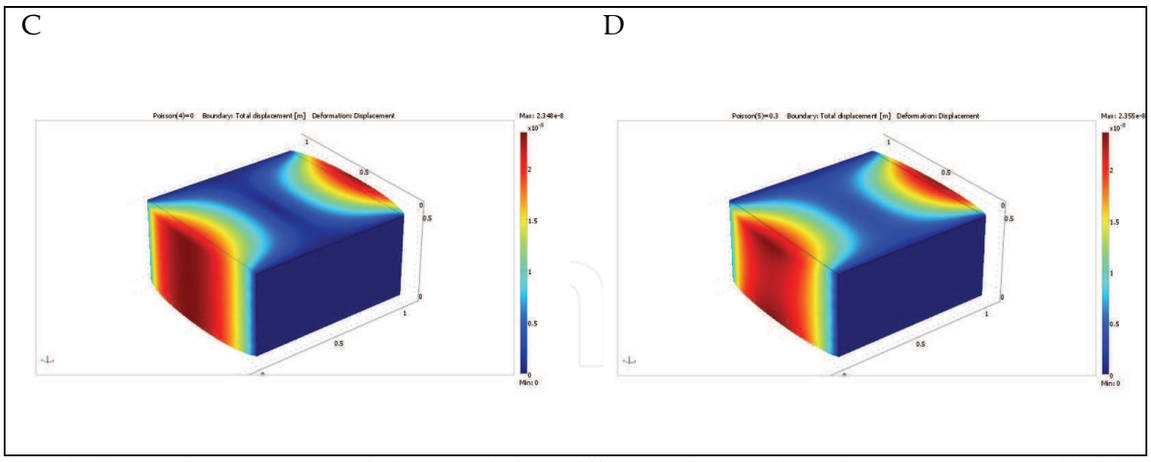

Fig. 9. Total displacement of the box-3 for different Poisson's ratios v: A) v = -0.999999, B) v = -0.7, C) v = 0, D) v = 0.3

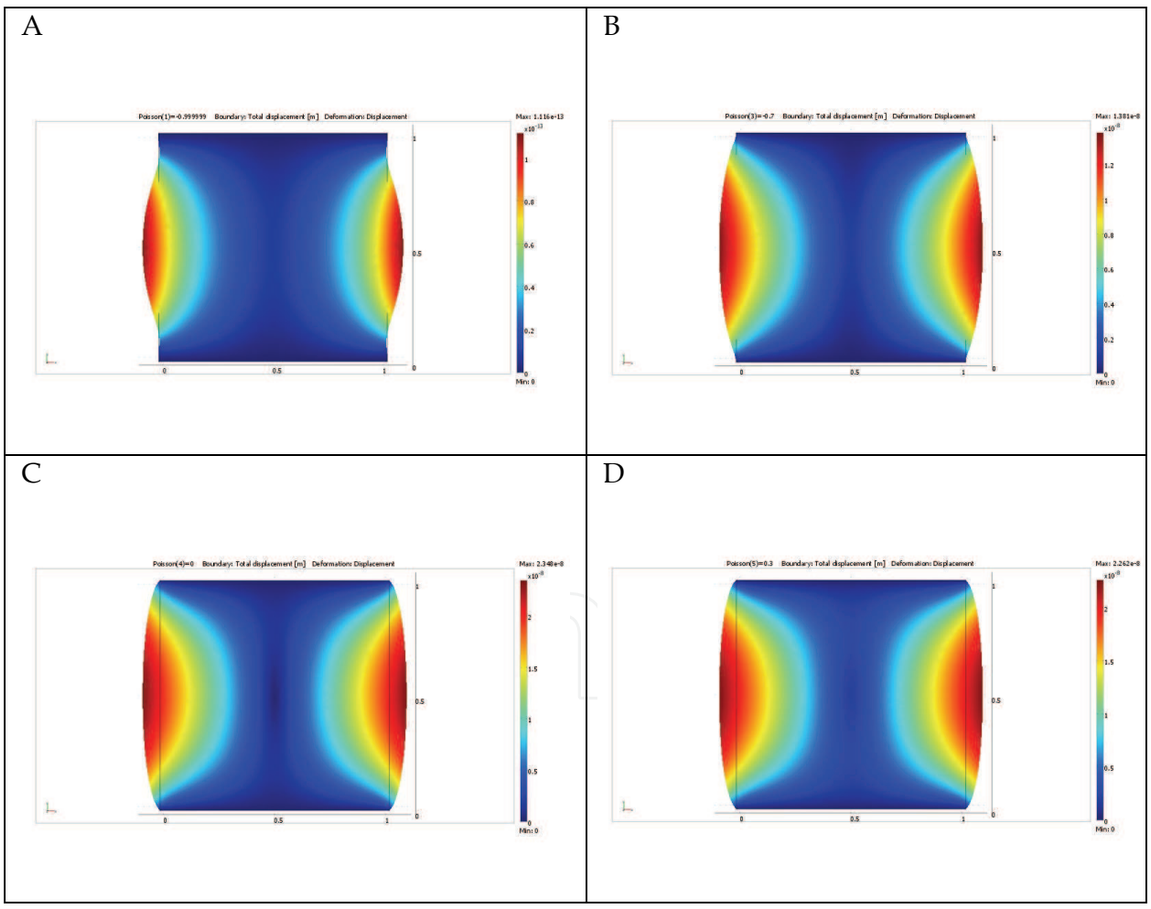

Fig. 10. XY-view of total displacement of the box-3 for different Poisson's ratios v: A) v = -0.999999, B) v = -0.7, C) v = 0, D) v = 0.3

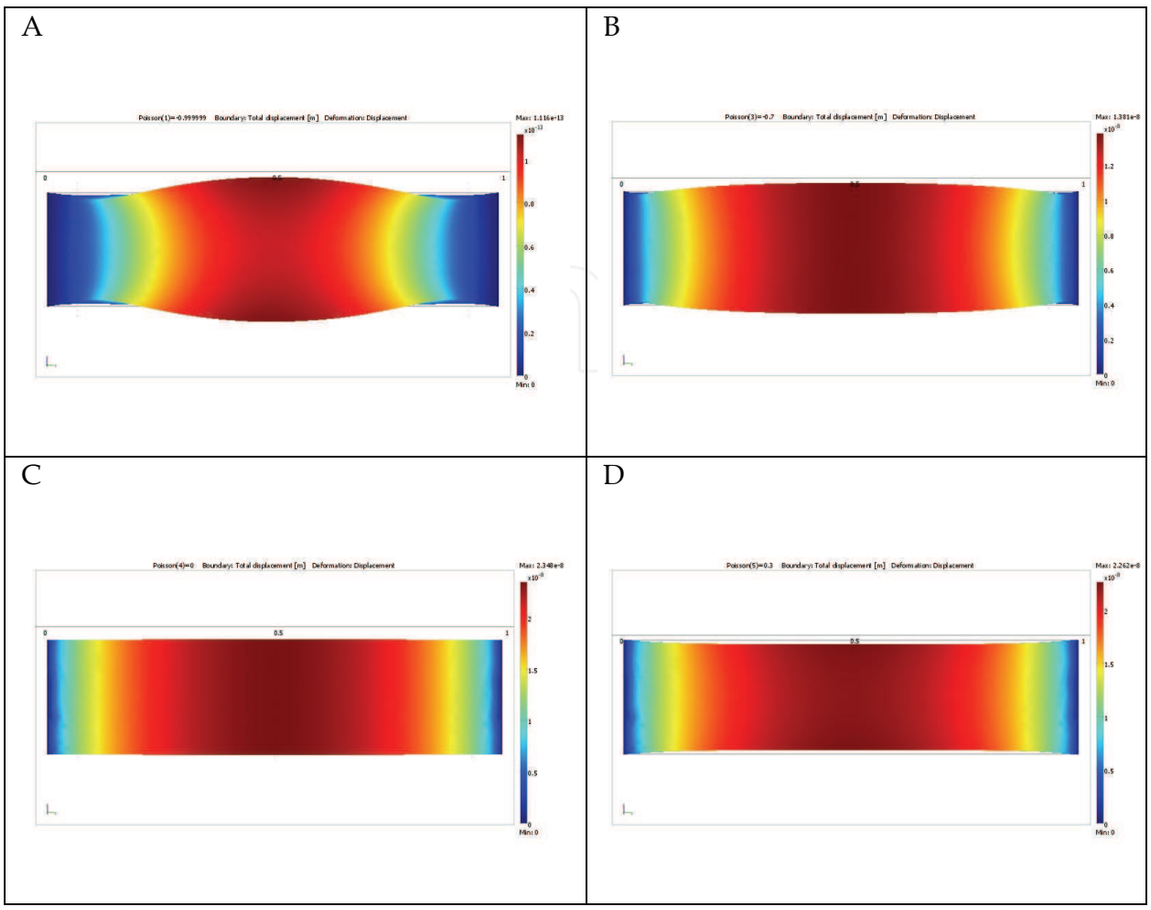

Fig. 11. YZ-view of total displacement of the box-3 for different Poisson's ratios ν: A) ν = -0.999999, B) ν = -0.7, C) ν = 0, D) ν = 0.3

The table below (Table 3) shows maximum value of the deformation on the surface to which the load is applied and average value of the deformation for different Poisson's ratios. One can see that with growing height, *h*, of the box for given Poisson's ratio and pressure the maximum deformation increases and the average deformation decreases. For a given shape of the box the maximum deformation increases with increasing Poisson's ratio.

	ν = -0.999999		ν = -0.7		ν = 0		ν = 0.3	
	Max.	Avg.	Max.	Avg.	Max.	Avg.	Max.	Avg.
Box-1	9.754e-14	3.557e-14	1.607e-8	8.585e-9	2.348e-8	1.772e-8	2.743e-8	1.635e-8
Box-2	9.371e-14	4.272e-14	1.536e-8	9.360e-9	2.348e-8	1.783e-8	2.567e-8	1.707e-8
Box-3	9.086e-14	4.898e-14	1.425e-8	9.729e-9	2.348e-8	1.783e-8	2.355e-8	1.713e-8

Table 3. Maximum and average total displacements of loaded boundaries of boxes

In Fig. 12 the deformation of the thinnest of the studied boxes is shown for the lowest Poisson's ratio and the finest mesh studied. Some oscillations of the loaded surface can be seen there. This new phenomenon, shown in more detail in Fig. 13, will be even better seen in the 2D case discussed in the next subsection.

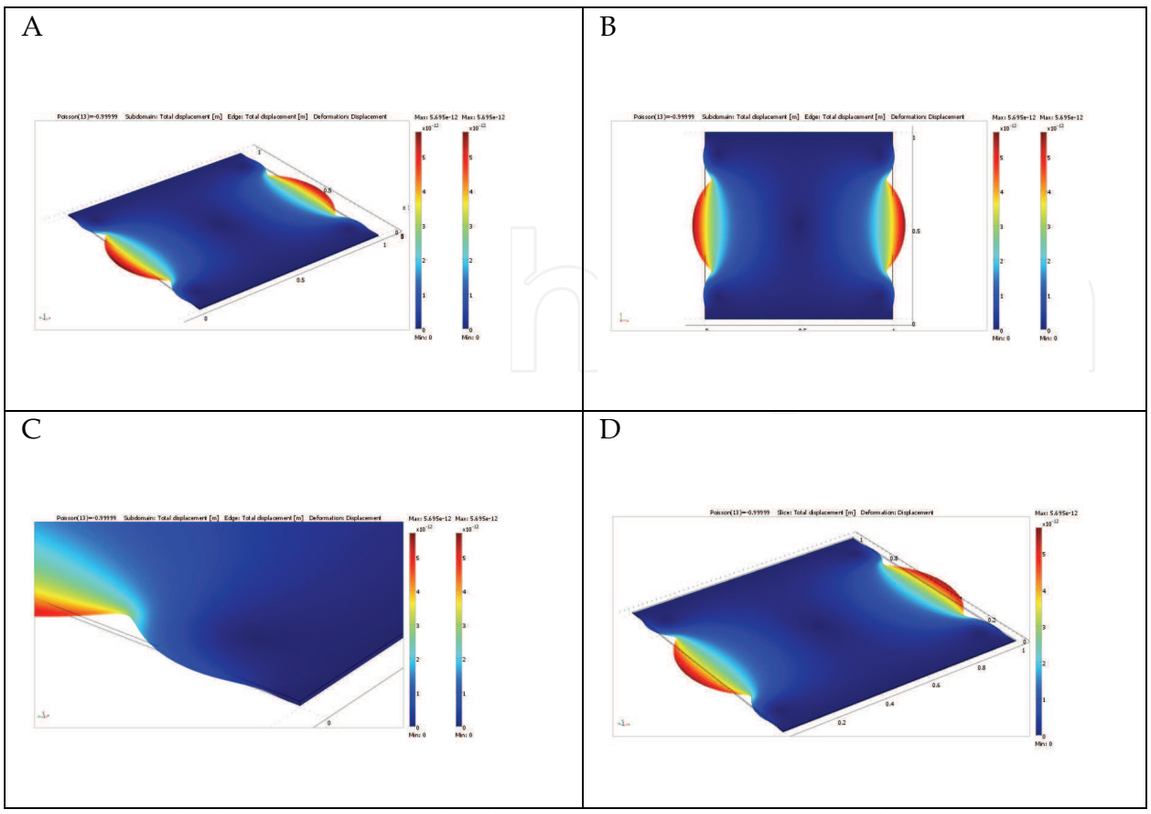

Fig. 12. Total displacement of the box-4 with different Poisson's ratio ν=-0.999999: A) XYZ-view, B) XY-view, C) corner view, D) slice at height h/2

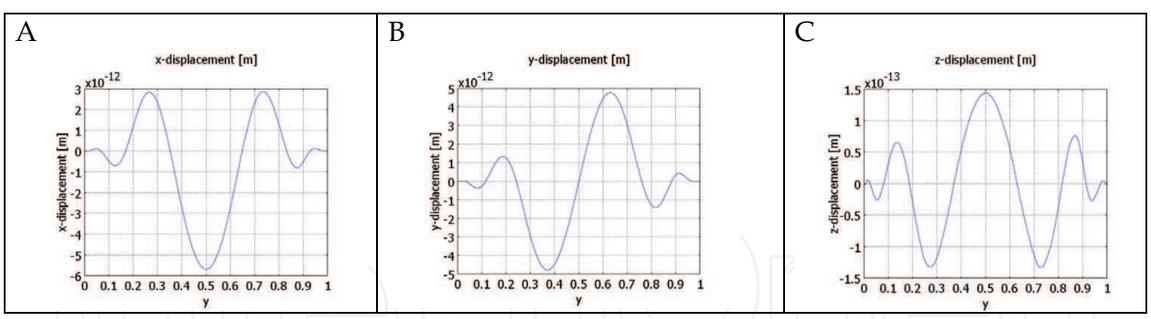

Fig. 13. Displacement of loaded edge (contact: loaded with free boundary) of box-4 with different Poisson's ratio ν=-0.999999: A) x-displacement, B) y-displacement, C) z-displacement

4.2 2D case

The object of our interest is a 2D linear elastic continuum, given through Young modulus E and Poisson's ratio ν. The domain is simply a unit square and is subjected to mixed boundary conditions. First type is kinematic type, often called Dirichlet type and the other is Neumann (or natural) type boundary condition responsible for the traction. The boundary conditions of the system (see Fig. 14) are the following:

- Loaded boundary $\Gamma_R : \boldsymbol{\sigma} \cdot \mathbf{n} = \mathbf{P}$,

- Loaded boundary $\Gamma_L : \boldsymbol{\sigma} \cdot \mathbf{n} = -\mathbf{P}$,
- Fixed boundaries Γ_T and $\Gamma_B : \mathbf{u} = \mathbf{0}$.

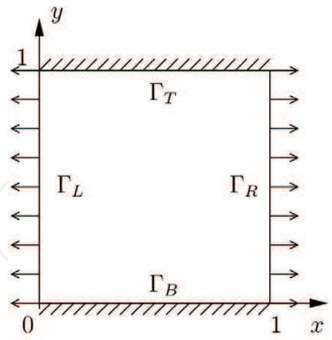

Fig. 14. Geometry of the system. Arrows indicate the uniform stretching force applied. Oblique lines indicate the fixed edges

To solve the problem, functions of the first order were taken as test and basis functions. It means that first order triangle Lagrange finite elements were taken. As the accuracy of finite element method depends on density of the mesh as well as on the degree of interpolating polynomial, the considered model was simulated with various mesh densities. Some calculations with higher order polynomials were also conducted and showed very good agreement with results obtained for first degree polynomials for dense enough meshes.

The most limiting factor in FEM computation is the memory, needed to store and solve systems of algebraic equations. Here, the upper limit of mesh density due to the limit of 32 GB RAM available was 15 600 000 triangle elements of first order with 7 845 601 points, what equals N=2800 intervals at a square side. The constants defining material and simulation conditions are as follows: E=2.1x10^{11} [N/m], $|P|=|\sigma_{xx}|=10^4$ [N/m] and ν varying from 0.7 down to -0.999.

The point of our interest will be only one component of the displacement field revealing the effect of interest. Fig. 15 shows details of the x-component of the displacement field u as function of y being position of the point on edge Γ_R . The x-component of displacement field is denoted by u_x .

As long as ν is non-negative (0.7, 0.0) the sign of u_x is the same as the sign of acting force, so the system behaves in a common way. But when ν takes the negative values (-0.7, -0.999) it is clear to observe that the u_x on some regions has negative values, what means that the body moves in opposite direction to the acting force!

In the case of $\nu = -0.7$ there is only one region on the boundary where the counterintuitive behavior is observed, but as ν tends to its lower limit (-1) and takes value -0.999 it is easy to notice that depending on mesh density the number of isolated negative-valued u_x varies from one (in case of N=250) to at least two (for N=2000). Obviously lower Poisson's ratio values need finer meshes to precisely track the behavior near corners of the square.

One would expect that there exist some critical value of ν when the counterintuitive effect occurs. In terms of FEM simulation this value strongly depends on the density of the mesh. To estimate convergence of the critical ν as function of the mesh density values, the values of $\nu_c(N)$ were computed for certain N and plotted in Fig. 16. It can be seen that $\nu_c(N)$ is an increasing function of N and is convex as a function of N^{-1} . The representation of $\nu_c(N)$ as

function N^{-1} takes the advantage of bringing infinity to zero and lets one to have a better view on the convergence. Looking at Fig. 16, one can state that

$$-.2 < \nu_c \equiv lim_{N->\infty}\, \nu_c(N)\,. \tag{21}$$

Observing the behavior of u_x for the case of $\nu = -0.999$ one expects existence of more points where u_x changes sign between positive and negative values when ν tends to -1.

It should be also stated that for the lowest studied ν the closer to the korner, the worse the convergence is. To study models with extremely low ν values, very dense meshes are essential and higher order interpolating polynomials should be also considered.

To make clear that counterintuitive results are reliable some cases were checked using another FEM libraries - GETFEM++, FREEFEM and ABAQUS. These showed exactly the same unusual behaviour of the system.

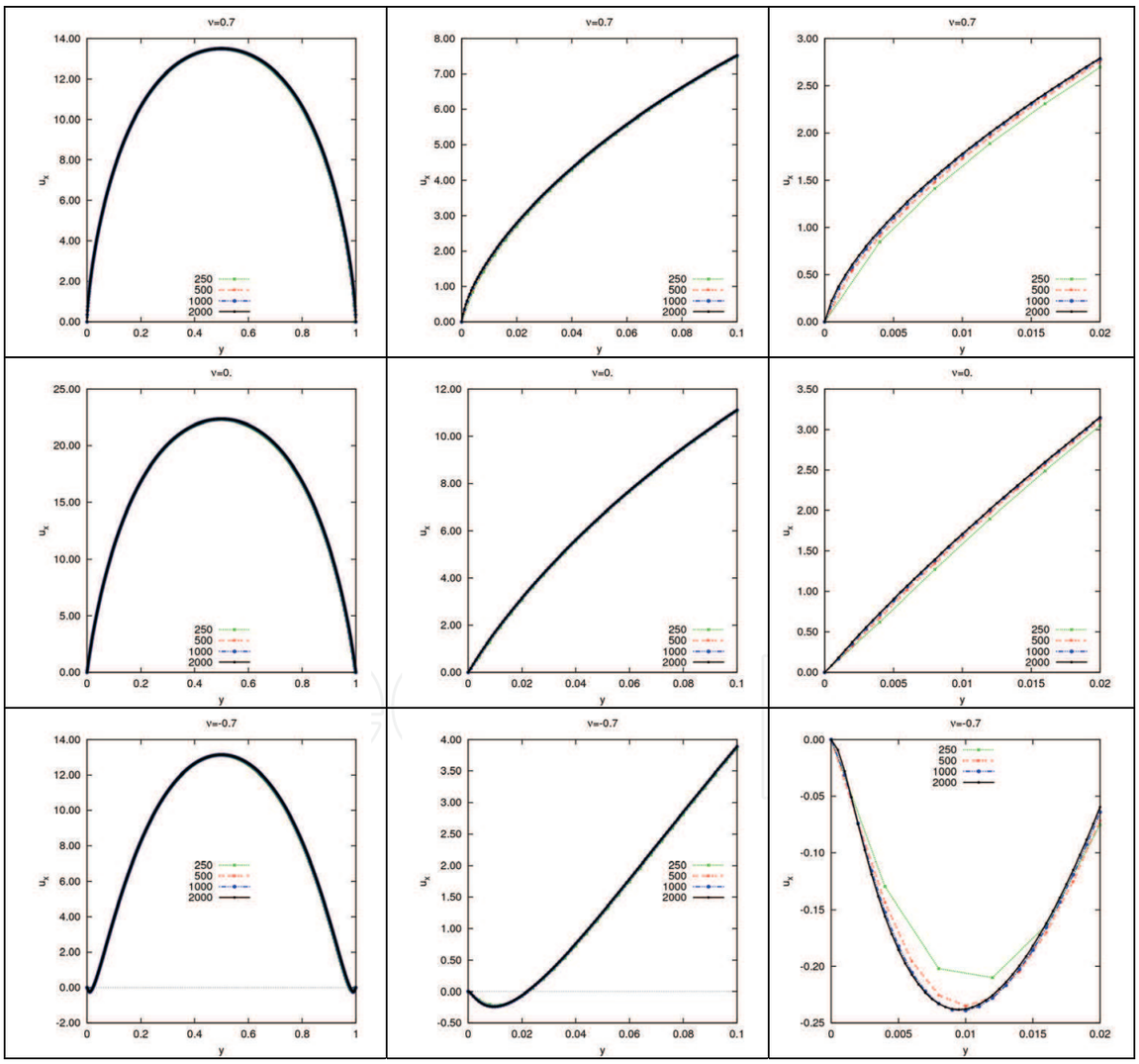

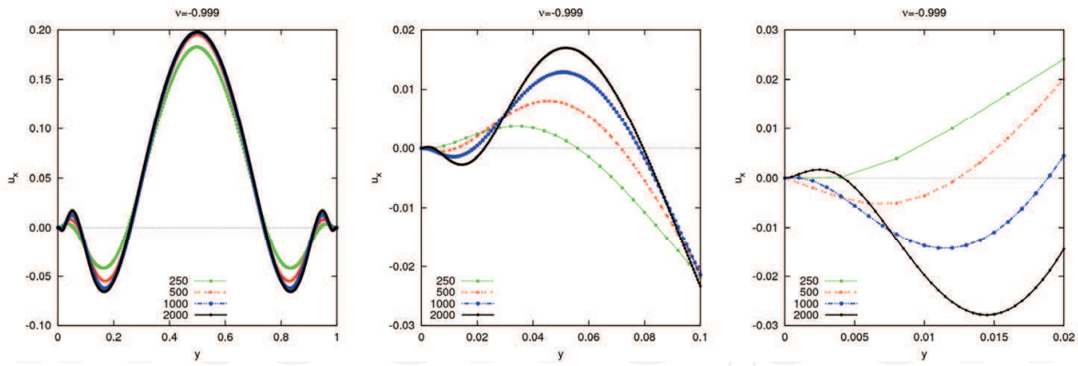

Fig. 15. u_x being the x-component of the displacement vector multiplied by 10^9 (with exception of the last figure in which the factor was 10^{10}) as a function of y for different Poisson's ratios. Figures show the dependence on the whole edge and its details near to the upper-right corner. The numbers in the legend describe the values of N for the meshes.

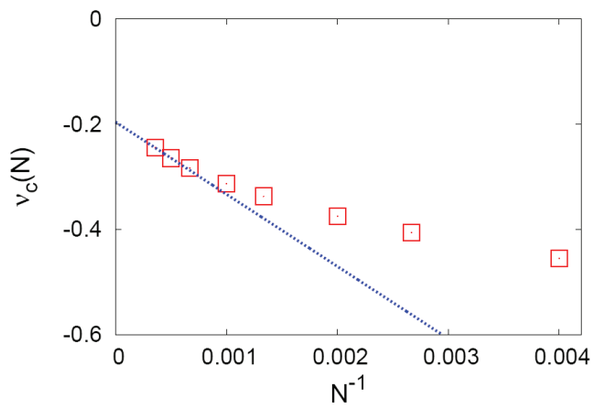

Fig. 16. The N^{-1} dependence of $\nu_c(N)$. The dotted line goes through the points corresponding to the two largest values of N=2000,2800.

5. Conclusions

In this chapter, results of studies described in (Strek et al., 2008) and (Poźniak et al., 2010) have been reviewed and extended. By considering simple 2D and 3D examples, it has been shown that constrained auxetics can exhibit (locally) negative compliance. This unusual effect – material moving in the direction opposite to the force acting – is observed in 2D near the corners of the deformed square whereas in 3D it can be seen near the edges of the fixed walls of the box. In 2D case, the calculations performed prove that the maximum Poisson's ratio for which such a behaviour is found is not less than -0.2. In 3D, the corresponding Poisson's ratio is not less than -0.7.

The obtained results do not contradict the closure presented in (Poźniak et al., 2010) that the critical Poisson's ratio for which such a behaviour can be observed is zero, i.e. *any* auxetic material in 2D and 3D may show locally negative compliance. Work is in progress to prove that hypothesis.

In 3D case the authors have determined the maximum deformation and the average deformation of the box for different shapes of the box and for different values of the

Poisson's ratio. It has been found that for a given Poisson's ratio the maximum deformation grows and the average deformation decreases with increasing height of the box. For a given box shape the maximum deformation increases with increasing Poisson's ratio.

6. Acknowledgements

This work was partially supported by the grant NN202 261438 MNiSW. Part of the simulations was carried out at the Poznan Supercomputing and Networking Center (PCSS).

7. References

Comsol (2004). Comsol Structures Mechanics Module, Femlab 3.1 User's Guide, Comsol AB.

Comsol (2007). Comsol Multiphisycs 3.4 User's Guide, Comsol AB.

Evans K.E. (1991). Auxetic polymers – a new range of materials, Endeavour 15, pp. 170-174.

Hartwig G. (1995). Support elements with extremely negative thermal expansion, Cryogenics Volume: 35, Issue: 11, Nonmetallic Materials, pp. 717-718.

Hinton E., Owen D.R.J. (1979). An Introduction to Finite Element Computations, Pineridge, Swansea.

Huebner K.H. (1975). The Finite Element Method for Engineers, Wiley, Toronto.

Jaglinski T., Kochmann D., Stone D., Lakes R. S. (2007). Materials with viscoelastic stiffness greater than diamond, Science 315, pp. 620-622.

Landau L. D., Lifshits E. M. (1986). Theory of elasticity, Pergamon Press, London.

Lakes R.S. (1987). Foam structures with a negative Poisson's ratio, Science , 235 pp.1038-1040.

Lakes R.S. (2001). Extreme damping in composite materials with a negative stiffness phase, *Phys. Rev. Lett.* 86, 2897-2900.

Lakes R. S., Lee T., Bersie A., Wang Y. C. (2001). Extreme damping in composite materials with negative-stiffness inclusions, Letters to Nature, Nature 410, pp. 565-567.

Lakes R., Wojciechowski, K. W. (2008). Negative compressibility, negative Poisson's ratio, and stability, *Phys. Stat. Solidi b*, 245, pp. 545-551.

Logg A., Wells G. N. (2010). DOLFIN: Automated finite element computing, ACM Transactions on Mathematical Software, 37(2).

Poźniak A.A., Kamiński H., Kędziora P., Maruszewski B., Stręk B., and Wojciechowski K.W. (2010). Anomalous deformation of constrained auxetic square, Reviews on Advanced Materials Science, 23, pp. 169-174.

Remillat C., Scarpa F, Wojciechowski K.W. (2009). Preface, Physica Status Solidi b, 246, pp. 2007-2009; (see also references there).

Ruppin R. (2000). Extinction properties of a sphere with negative permittivity and permeability, Solid State Communications 116, pp. 411-415.

Sang Z.-F., Li Z.-Y. (2005). Effective negative refractive index of graded granular composites with metallic magnetic particles, Physics Letters A, Volume: 334, Issue: 5-6, January 24, pp. 422-428.

Strek T., Maruszewski M., Narojczyk J., Wojciechowski K.W. (2008). Finite element analysis of auxetic plate deformation, Journal of Non-Crystalline Solids, 354, pp. 4475–4480.

Zienkiewicz O. C., Taylor R. L. (2000). The Finite Element Method, Volume 1-3, (Fifth edition) Butterworth-Heinemann, Oxford.

Finite Element Analysis

Edited by David Moratal

ISBN 978-953-307-123-7

Hard cover, 688 pages

Publisher Sciyo

Published online 17, August, 2010

Published in print edition August, 2010

Finite element analysis is an engineering method for the numerical analysis of complex structures. This book provides a bird's eye view on this very broad matter through 27 original and innovative research studies exhibiting various investigation directions. Through its chapters the reader will have access to works related to Biomedical Engineering, Materials Engineering, Process Analysis and Civil Engineering. The text is addressed not only to researchers, but also to professional engineers, engineering lecturers and students seeking to gain a better understanding of where Finite Element Analysis stands today.

InTech Europe

University Campus STeP Ri
Slavka Krautzeka 83/A
51000 Rijeka, Croatia
Phone: +385 (51) 770 447
Fax: +385 (51) 686 166
www.intechopen.com

InTech China

Unit 405, Office Block, Hotel Equatorial Shanghai
No.65, Yan An Road (West), Shanghai, 200040, China
中国上海市延安西路65号上海国际贵都大饭店办公楼405单元
Phone: +86-21-62489820
Fax: +86-21-62489821

IntechOpen